AIP | Review of Scientific Instruments

The development and deployment of a ground-based, laser-induced fluorescence instrument for the in situ detection of iodine monoxide radicals

M. E. Thurlow, D. T. Co, A. S. O'Brien, R. A. Hannun, L. B. Lapson, T. F. Hanisco, and J. G. Anderson

Citation: Review of Scientific Instruments **85**, 044101 (2014); doi: 10.1063/1.4869857
View online: http://dx.doi.org/10.1063/1.4869857
View Table of Contents: http://scitation.aip.org/content/aip/journal/rsi/85/4?ver=pdfcov
Published by the AIP Publishing

The development and deployment of a ground-based, laser-induced fluorescence instrument for the *in situ* detection of iodine monoxide radicals

M. E. Thurlow,[1,a)] D. T. Co,[1,2] A. S. O'Brien,[1,3] R. A. Hannun,[1] L. B. Lapson,[1] T. F. Hanisco,[1,4] and J. G. Anderson[1]

[1]*Department of Chemistry and Chemical Biology, Harvard University, 12 Oxford Street, Cambridge, Massachusetts 02138, USA*

[2]*Argonne-Northwestern Solar Energy Research Center and Department of Chemistry, Northwestern University, 2145 Sheridan Road, Evanston, Illinois 60208-3113, USA*

[3]*Department of Civil and Environmental Engineering, Princeton University, Princeton, New Jersey 08544, USA*

[4]*NASA Goddard Space Flight Center, Code 614, Greenbelt, Maryland 20771, USA*

(Received 17 January 2014; accepted 17 March 2014; published online 17 April 2014)

High abundances of iodine monoxide (IO) are known to exist and to participate in local photochemistry of the marine boundary layer. Of particular interest are the roles IO plays in the formation of new particles in coastal marine environments and in depletion episodes of ozone and mercury in the Arctic polar spring. This paper describes a ground-based instrument that measures IO at mixing ratios less than one part in 10^{12}. The IO radical is measured by detecting laser-induced fluorescence at wavelengths longer that 500 nm. Tunable visible light is used to pump the $A^2\Pi_{3/2}$ ($v' = 2$) $\leftarrow$ $X^2\Pi_{3/2}$ ($v'' = 0$) transition of IO near 445 nm. The laser light is produced by a solid-state, Nd:YAG-pumped Ti:Sapphire laser at 5 kHz repetition rate. The laser-induced fluorescence instrument performs reliably with very high signal-to-noise ratios (>10) achieved in short integration times (<1 min). The observations from a validation deployment to the Shoals Marine Lab on Appledore Island, ME are presented and are broadly consistent with *in situ* observations from European Coastal Sites. Mixing ratios ranged from the instrumental detection limit (<1 pptv) to 10 pptv. These data represent the first *in situ* point measurements of IO in North America. © *2014 AIP Publishing LLC*. [http://dx.doi.org/10.1063/1.4869857]

I. INTRODUCTION

Recent studies of atmospheric iodine suggest that it is important to broad ranging aspects of atmospheric chemistry with significant potential impacts on human health and climate. Figure 1 highlights the various roles of iodine photochemistry in the atmosphere. First, laboratory studies[1–4] and atmospheric observations[5–15] imply that iodine contributes to the formation and growth of particles in the marine boundary layer (MBL). Second, atmospheric iodine may facilitate the oxidation of elemental mercury to a bioavailable form that can accumulate in ecosystems.[16,17] Finally, reactive iodine can influence the oxidative capacity of the atmosphere through the catalytic destruction of ozone[18–21] and the conversion of HO_2 to OH.[18,22,23,84] A recent review by Saiz-Lopez *et al.*[24] details the current state of understanding of atmospheric iodine chemistry.

The sources of reactive iodine in the atmosphere are short-lived iodocarbons (e.g., CH_3I and CH_2ClI) and molecular iodine, which have mixing ratios of a few parts per trillion (pptv, equivalent to pmol mol^{-1}) in the MBL.[13,25–28] In recent years, emissions of reactive iodine precursors from macroalgae in coastal regions have been studied extensively,[13,26,29–31] but these sources likely represent a small fraction of emissions on the global scale.[24] In contrast, sources of organic and inorganic iodine over the open ocean are neither well understood nor well quantified.[24] Recent laboratory studies suggest that hypoidous acid (HOI) is an important source of atmospheric iodine,[32] but current analytical techniques are inadequate for measuring ambient concentrations of HOI. Once in the atmosphere, these very short-lived sources of iodine are readily photolyzed to form atomic iodine, which then reacts with O_3 to form iodine monoxide (IO):

$$RI + h\nu \rightarrow R + I, \tag{1a}$$

$$I_2 + h\nu \rightarrow I + I, \tag{1b}$$

$$I + O_3 \rightarrow IO + O_2. \tag{2}$$

These reactions are known to produce significant amounts of reactive iodine (pptv of IO, OIO, HOI) in the MBL,[33,34,41] but longer-lived species (e.g., CH_3I) may be transported to the higher altitudes by convective transport.[20,35]

Despite the potentially important roles played by IO in the various facets of atmospheric photochemistry, the database of available measurements to characterize the distribution of reactive iodine is limited. The majority of measurements have been made using spatially averaged techniques based on differential optical absorption spectroscopy (DOAS), including long-path

a)Author to whom correspondence should be addressed. Electronic mail: thurlow@huarp.harvard.edu

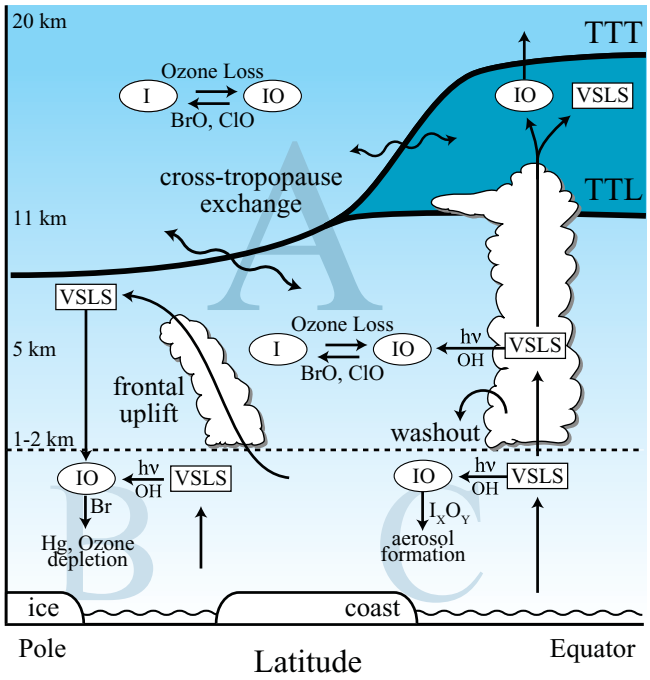

FIG. 1. The different facets of iodine photochemistry in the atmosphere initiated from very short-lived source gases (VSLS): (A) ozone depletion, (B) Arctic Mercury Depletion Episodes (AMDE), and (C) coastal new particle and cloud condensation nuclei (CCN) formation. The transport of iodine across the tropopause (TTT = Thermal Tropical Tropopause, TTL = Tropical Tropopause Layer) does not lead to widespread elevation in IO concentrations in the stratosphere.

(LP-DOAS)[6,9,13,14,33,34,36–40] and multi-axis (MAX-DOAS) observations.[42–47] Available *in situ* measurements by laser-induced fluorescence (LIF)[8,10,48] and cavity ringdown spectroscopy (CRDS)[7] show significantly higher maximal concentrations of IO than spatially averaged measurements. In an instrumental intercomparison, Commane *et al.*[48] reported that LIF measurements were as much as an order of magnitude higher than the DOAS measurements. The presence of "hot spots" that are highly episodic and spatially inhomogeneous suggests that *in situ* observations are critical for understanding the relevance of IO to nucleation events[1] and radical chemistry, which may be sensitive to variations in abundance on short spatial scales.

A global-scale climatology of reactive iodine requires a diverse database of measurements. Most direct observations of reactive iodine and its precursors have occurred in a relatively narrow range of mid latitude coastal sites (e.g., Mace Head, Ireland and Roscoff, France). Ship-based observations by MAX-DOAS have only recently been reported from the eastern[49] and western[43] Pacific Ocean. The satellite-based Scanning Imaging Absorption Spectrometer for Atmospheric Chartography (SCIAMACHY) provided global coverage, but absolute column densities and spatial distributions proved to be sensitive to the assumptions of the retrieval algorithms used to interpret the observations.[50,51] Direct, vertically resolved measurements of IO are necessary to provide constraints for improving future retrievals of satellite observations.

Highly sensitive *in situ* measurements are also critical for probing local concentrations of IO to determine its contribution to ozone destruction throughout the free troposphere and lower stratosphere. The abundance of CH_3I, a relatively stable photochemical precursor of IO, is known to be variable above the boundary layer and strongly dependent on local convection (e.g., Refs. 52 and 53), which suggests that IO concentrations may be highly variable as well. IO is not ubiquitous in the lower stratosphere[54–57] but may be significant locally.[46] Though no *in situ* measurements in the free troposphere exist, MAX DOAS measurements of the slant column density of IO have been made recently at a high altitude observatory[47] and by aircraft.[45] Both observations show detectable levels of IO at high altitude. Dix *et al.*[45] suggest that more than half of the vertical column abundance of IO may exist above the boundary layer in the tropical free troposphere. The possibility that IO may be widespread throughout the free troposphere is significant: (1) It suggests that the sources and sinks of IO may not be fully understood; (2) It challenges the assumption that IO is localized to the boundary layer, which serves as a basis for the interpretation of satellite observations;[50,51] (3) It suggests that IO may influence tropospheric ozone. A modeling study based on observations of reactive halogens and precursors suggested the halogen-mediated ozone depletion accounts for 15%-30% of ozone loss integrated over the total tropospheric column in the tropics.[35] Inclusion of iodine chemistry in the model led to a 4-fold increase in halogen-mediated ozone loss relative to bromine alone. These observations and modeling results motivate future vertically resolved measurements of IO *in situ* throughout the free troposphere and into the lower stratosphere.

The inhomogeneity of IO in the atmosphere requires a mobile *in situ* instrument to target regions that contain significant IO photochemistry. This paper describes the development and calibration of an IO instrument based on LIF detection, which has been used extensively by this laboratory for measuring free radicals *in situ* in the free troposphere and stratosphere.[58–61] The IO instrument was designed and tested for ground-based measurements with the capability of becoming deployable in future aircraft- and ship-borne campaigns. Preliminary measurements taken at the Shoals Marine Laboratory on Appledore Island, ME are presented. IO measurements with sub-pptv sensitivity are demonstrated with short integration times (~1 min).

II. LIF AND THE DETECTION OF ATMOSPHERIC IO

The detection of IO by LIF has been successfully demonstrated by several groups (e.g., Refs. 8, 62–65). The (v′, 0), v′ = 0, 1, 3, 4, and 5, bands of the $A^2\Pi_{3/2} \leftarrow X^2\Pi_{3/2}$ transition of IO do not exhibit structure in their absorption spectra. The $A^2\Pi_{3/2}$ states of these bands have a short lifetime due to spin-orbit coupling between the excited state and one or more $\Omega = 3/2$ repulsive states.[66] A near-cancellation of the overlap of bound and continuum wavefunctions at $v' = 2$ provides a comparatively slow predissociation at that level, giving rise to narrow rotational absorption features (FWHM ~ 0.04 cm^{-1}) suitable for LIF excitation. The laser-induced fluorescence excitation spectrum was measured for this work and is shown in

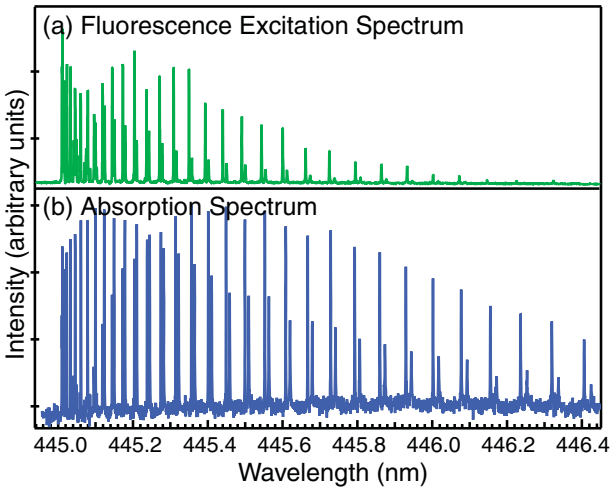

FIG. 2. (a) IO fluorescence excitation spectrum measured in this work and (b) the rotationally resolved absorption spectrum of the (2,0) band of the $A^2\Pi_{3/2} \leftarrow X^2\Pi_{3/2}$ transition.[54]

Figure 2 along with the rotationally resolved absorption spectrum of the (2,0) band of the $A^2\Pi_{3/2} \leftarrow X^2\Pi_{3/2}$ transition of IO reported by Wennberg *et al.*[54]

Dissociation of IO in the $v' = 2$ level of the $A^2\Pi_{3/2}$ electronic state becomes increasingly competitive with fluorescence as higher J states are excited. The lifetime for the excited state of IO is short: ~1 ns for $J' = 1.5$ decreasing to 15 ps for $J' = 50.5$.[66] Collisional quenching of the $v' = 2$ rotational states in N_2 was characterized by Gravestock *et al.*[67] The inferred rate constant of quenching (k_q) for the bandhead (a mixture of $J' = 3.5$, 4.5, and 5.5 states) was $k_q = 9.6 \pm 6.3 \times 10^{-11}$ cm^3 mol^{-1} s^{-1} and increased at higher pressures and J' values. Excitation to the $J' = 7.5$ state of the (2,0) band around 445 nm was selected as the basis for detection in this work. Using k_q from the bandhead, a reasonable approximation for the conditions used in this study ($J' = 7.5$, 20 Torr) yields a quenching lifetime (τ_q) of 16 ns and a fluorescence lifetime (τ_f) of 0.5 ns.

Figure 3(a) shows the excitation and fluorescence scheme employed in this work. The spectrally resolved fluorescence emission resulting from the excitation of IO at 445 nm (20 Torr) was collected using a 1-m focal length multi-pass Ebert spectrometer (Jarrell Ash, Boston, MA). The spectrum was then corrected for the quantum efficiency of the photomultiplier tube (PMT) at different wavelengths and is shown in Figure 3(b). The fluorescence signal corresponds to the vibrational bands of the $A^2\Pi_{3/2}$ ($v' = 2$) → $X^2\Pi_{3/2}$ ($v'' = 0$–11) transitions, confirming that vibrational relaxation is a negligible channel compared to fluorescence. The relative intensities of the vibrational bands agree well with published Franck-Condon factors.[68] In the IO instrument described here, a 530 nm bandpass filter (Semrock FF01-530/23-25, Rochester, NY) and 514 nm longpass filter (Semrock LP02-514RE-25, Rochester, NY) are used to capture the fluorescence from the $v' = 2 \rightarrow v'' = 5$ and $v'' = 6$ transitions as indicated in Figure 3(b). These two bands constitute 16% of the total fluorescence intensity arising from the $v' = 2$ state.

To maximize the specificity of the IO measurement, the laser is tuned across the R7.5 line (445.033 nm, "online") and then to an off- resonance wavelength ("offline") between the R6.5 and R7.5 absorption features (445.028 nm). The difference between the signals at the two frequencies is used to determine the IO mixing ratio. The online frequency has a large differential cross section (2.92×10^{-16} cm^2 mol^{-1}) and the offline frequency is characterized by a broad, clean baseline at the pressure used for detection (20 Torr). The online and offline frequencies were selected to minimize the differential absorption cross section of NO_2, which has structured absorption features in this wavelength region and can be present at high concentrations in the atmosphere. The differential cross section between the online and offline wavelengths is small (<3%) for NO_2. Additionally, since the fluorescence of NO_2

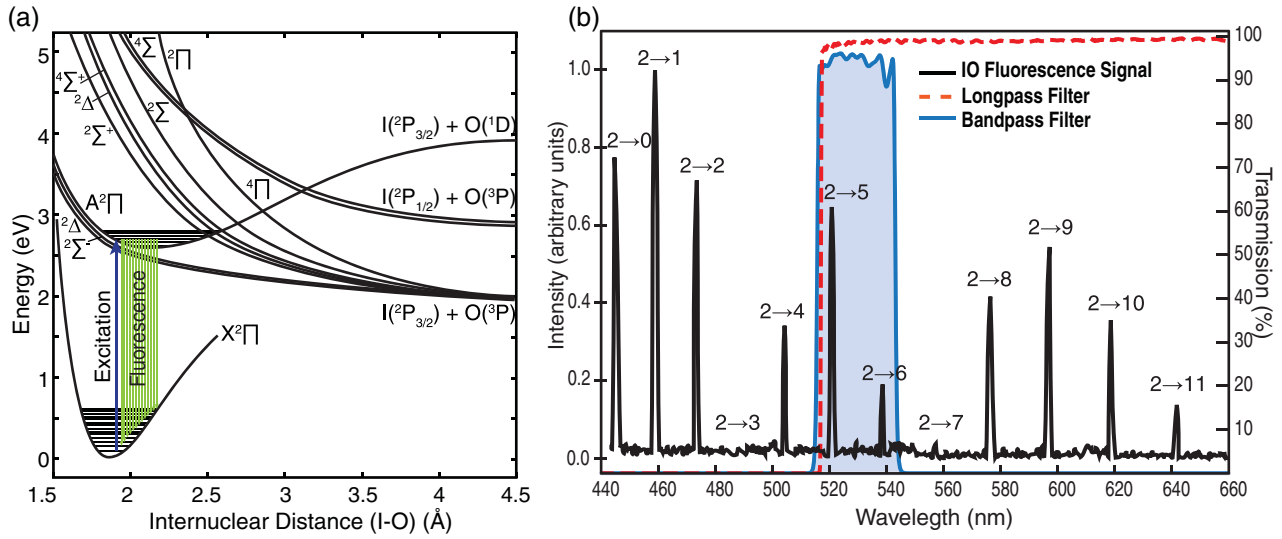

FIG. 3. The LIF detection of IO. (a) IO is pumped via a ro-vibronic transition of the $A^2\Pi_{3/2}$ ($v' = 2$) ← $X^2\Pi_{3/2}$ ($v'' = 0$) band near 445 nm. Red shifted fluorescence is observed. (b) The peaks correspond to the vibrational bands of the $A^2\Pi_{3/2}$ ($v' = 2$) → $X^2\Pi_{3/2}$ ($v'' = 0$–11) transitions. Vibrational energy transfer to $v' = 0$ or 1 was not observed. The fluorescence from the $A^2\Pi_{3/2}$ ($v' = 2$) → $X^2\Pi_{3/2}$ ($v'' = 5$-6) transitions is collected for the IO instrument using a combination of a bandpass and longpass filter to reject short- and long-wave interferences.

TABLE I. Differences between Harvard and Leeds LIF Instruments.

Instrument feature	This work	Whalley *et al.*[8]
Max laser power at 445 nm	80 mW	150 mW
Detection axis	32-pass white cell	Single pass cell
Online detection strategy	Tuning across R7.5 line	Online acquisition at a single frequency
Pressure of detection	20 Torr	150 Torr
Obs. fluorescence bands	(2,5) and (2,6) bands	(2,5) band
Reference cell	Yes	Not during deployment
Sensitivity	0.3 pptv in 60 s	0.3 pptv in 300 s

occurs over a broad range of frequencies, the use of long-pass and band-pass filters significantly reduces its contribution to the count rates observed both online and offline. No detectable contribution of NO_2 interference to the IO signal was observed during laboratory testing of up to 300 ppbv of NO_2. Interferences from chemical pathways that could produce IO within the instrument were also explored and found to be negligible (see Sec. S1 of the supplementary material[69]).

III. INSTRUMENT DESCRIPTION

The IO instrument was designed as a first generation ground-based/mobile sensor that is automated and integrated into an electronic architecture compatible with a broad range of field deployment methods. This section provides a detailed description of the hardware. Numerous considerations had to be addressed during the design process:

Sampling. The optimal design would draw sampled air to the detection axis in an essentially "wall-less" manner. IO radicals are extremely reactive and are lost efficiently to internal surfaces. A reduced pressure detection axis is used in which the distance between the inlet and detection region are minimized to meet these criteria and minimize losses.

Laser subsystem. A narrow-bandwidth tunable visible laser is required. High pulse repetition rates with average power greater than 20 mW are needed to make high signal-to-noise measurements of the sub-pptv mixing ratios of IO in the atmosphere. The laser subsystem is a nanosecond Nd:YAG pumped Titanium:Sapphire laser with a compact footprint.

Detection axis. The fluorescence detection axis was designed to allow large throughput while heavily discriminating against solar scatter and laser scatter. The detection axis selected is a 32-pass White cell with optical baffling and spectral filtering analogous to the Harvard NO_2 instrument detection axes.[60]

Data acquisition. The ground-based version of the IO instrument is expected to work for hours with minimal human interaction. Programs for data acquisition and experimental control were written in LabVIEW (National Instruments, Austin, TX) with error recovery capabilities.

Future integration. The IO instrument was designed with the capability to be integrated with the existing Harvard ClO[70] and BrO[71] flight instruments. As a result, the detection duct is identical to the halogen instruments used for airborne measurements by our group.

The instrument described in this work draws on similar fundamental spectroscopy as the LIF instrument deployed previously by the University of Leeds.[8,10,48] Major differences between the instruments are emphasized in Table I. The focus of the design process for this instrument was to increase specificity, time response, and mobility to enable sub-pptv measurements of IO with spatial and temporal resolution not obtained previously.

A. Sampling

IO is sampled using the fluorescence assay by gas expansion (FAGE) technique, a common technique for sampling free radicals in the atmosphere.[72] The sampling assembly is presented in Figure 4. The inlet consists of a flat plate with a 0.75 mm pinhole aperture for baric filtering and a 5.08 cm $\times$ 5.08 cm $\times$ 35 cm long duct, which delivers the reduced-pressure sample to the detection axis. A scroll vacuum pump (Varian Triscroll 600, Palo Alto, CA) is used to draw the sample through the inlet and into the detection axis. Flow rates of the sample through the system are typically 5 standard liters per minute. Laboratory tests of the pinhole inlet were

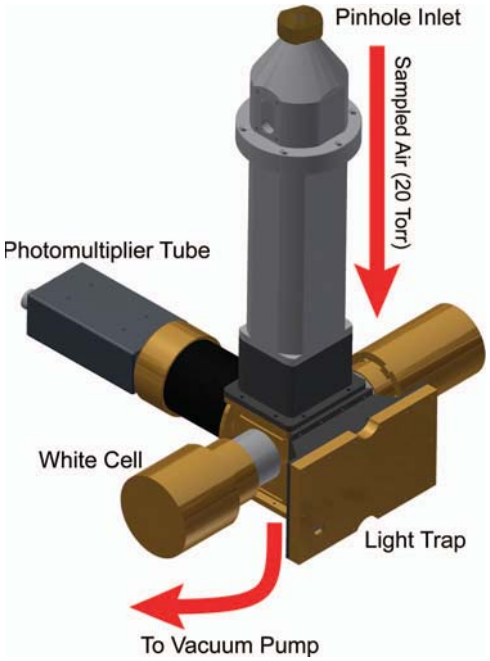

FIG. 4. Airflow within the IO instrument. Air enters the duct through a pinhole aperture, which reduces the pressure of the sample to 20 Torr. The sample then flows directly to the detection axis where a White cell, photomultiplier tube, optical filters, and an optical light trap are used to detect the fluorescence signal. The sample is exhausted through a vacuum pump.

conducted with a modular cavity ringdown detection axis placed in front of the pinhole aperture. These experiments enabled a direct measurement of the transmission efficiency of IO as it passed through the inlet to the detection axis of 83% ± 4%. The transmission efficiency of the pinhole aperture was higher than that of a molecular beam skimmer of the same diameter (77% ± 5%), which is another commonly used critical orifice in FAGE instruments.

B. Laser subsystem

A tunable, narrow-linewidth Ti-Sapphire laser (Photonics Industries DC150-532/Tu-H, Bohemia, NY) was custom built as the excitation source for the IO LIF instrument. A schematic of the optical design of the Ti: Sapphire system is presented in Figure 5. A Q-switched Nd:YAG laser at 532 nm (3.2 W average power at 5 kHz) pumps the Ti:Sapphire cavity. The wavelength of the laser is selected by tuning the angle of a diffraction grating (2000 lines/mm). The fundamental of the Ti:Sapphire (~890 nm) is doubled with a lithium triborate crystal to produce the 445 nm excitation wavelength used in this experiment. The Ti:Sapphire system produces an average power at 445 nm of approximately 80 mW at 5 kHz with 40 ns pulse widths. The high repetition rate of the laser yields relatively low per pulse energies ($<1.6 \times 10^{-5}$ J), reducing the likelihood of saturation in the excitation of IO. The upper limit of the linewidth of the Ti:Sapphire, as determined from laboratory measurements of IO and NO_2 absorption spectra at 20 Torr, was less than 0.05 cm^{-1}, consistent with the theoretical linewidth of 0.03 cm^{-1}. The laser linewidth is well matched to the linewidth of the R7.5 absorption feature (0.04 cm^{-1}) used for the detection of IO. The Ti:Sapphire and Nd:YAG pump laser have been integrated into a single, compact optical package with a 32 cm × 32 cm × 13 cm volume.

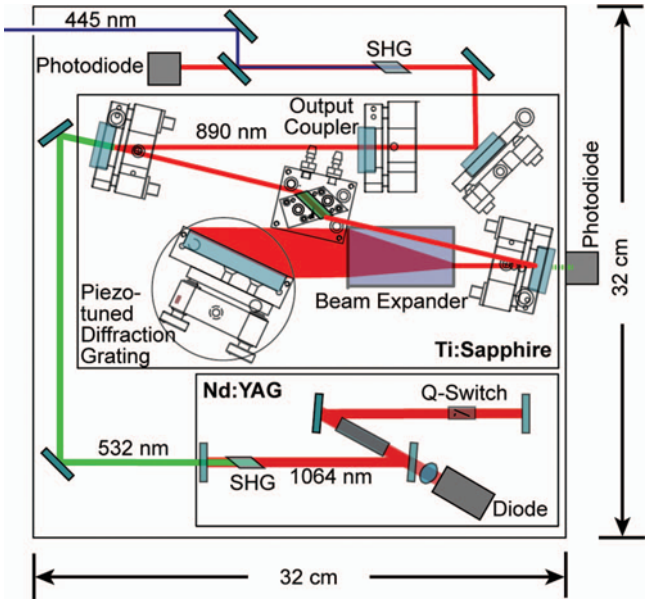

FIG. 5. Schematic of the pulsed visible Ti:Sapphire laser system. The Ti:Sapphire laser is powered by a single frequency-doubled Nd:YAG laser. The 890 nm output is then frequency-doubled to 445 nm. The footprint of the laser system is 32 cm × 32 cm.

Several modifications to the laser system have been made to improve its stability in the field and to aid in the analysis of laser performance. First, thermo-electric cooling modules (Laird Technologies CP2-31-06-L1, London, England) have been installed to improve thermal stability of the laser baseplate. Second, custom-built silicon photodetectors were implemented to monitor the output power of the Nd:YAG at 532 nm and the fundamental of the Ti:Sapphire at 890 nm. Third, a solenoid-driven laser shutter was incorporated to collect laser-free background counts during data acquisition. Finally, a piezo-driven rotation stage (Physik Instrumente M-035.ps, Germany) was implemented in place of a stepper motor for wavelength tuning. The piezo-driven rotation stage improves the speed and reliability of wavelength tuning. The minimum increment of wavelength tuning with the piezo-driven stage is 0.01 cm^{-1}. A custom-designed circuit provides stable, filtered voltages to the piezo element and monitors the position of the piezo with high sensitivity measurements from the integrated strain gauge sensor. This strain gauge signal serves as a convenient metric for the optical frequency of the laser.

C. Detection axis

The Ti:Sapphire laser output is directed to the detection axis by several turning mirrors on the optical breadboard. A multi-pass White cell, depicted in Figure 6(a), is configured so that the laser makes 32 passes through the detection volume before exiting. The White cell mirrors (Spectrum Thin Films, Bohemia, NY) are spaced at 15.5 cm with a reflectivity of >99.99% at 445 nm. The individual laser beams are expanded as they pass through the detection volume and are non-overlapping in space (see Figure 6(a)), reducing the potential for saturation in the absorption step. The entrance mirror of the White cell is sealed with an AR-coated glass window. Typically 90% of the incident laser power is transmitted through the cell. A small purge of nitrogen (~100 standard cubic cm per minute (sccm) per mirror) is introduced at the entrance and twin mirrors to maintain mirror cleanliness during sampling. The detection axis is baffled to reduce interference from laser and solar scatter. Knife-edge baffles line the walls and the region between the White cell mirrors and the detection volume. The baffles and the chamber walls are painted with a black paint selected to minimize fluorescence (Zuel, St. Paul, MN), and an optical trap is situated perpendicular to the propagation of laser light and directly opposite the detector to reduce chamber scatter.

A series of lenses and filters (Figure 3(b)) are used to direct fluorescence from the 1.5 cm × 2 cm × 3 cm volume in the center of the detection axis onto the gallium arsenide phosphide photocathode of the PMT (Hamamatsu Photonics H7421-40, Japan), which operates in photon-counting mode. On average, the solid angle collected by this lens system is 2.5% of 4π. The PMT was selected due to its high quantum efficiency (~38%) at the fluorescence collection frequencies and somewhat lesser quantum efficiency (25%) at the laser excitation wavelengths. The PMT is actively cooled to 0°C with thermoelectric coolers to reduce dark counts (typically <20 counts per second).

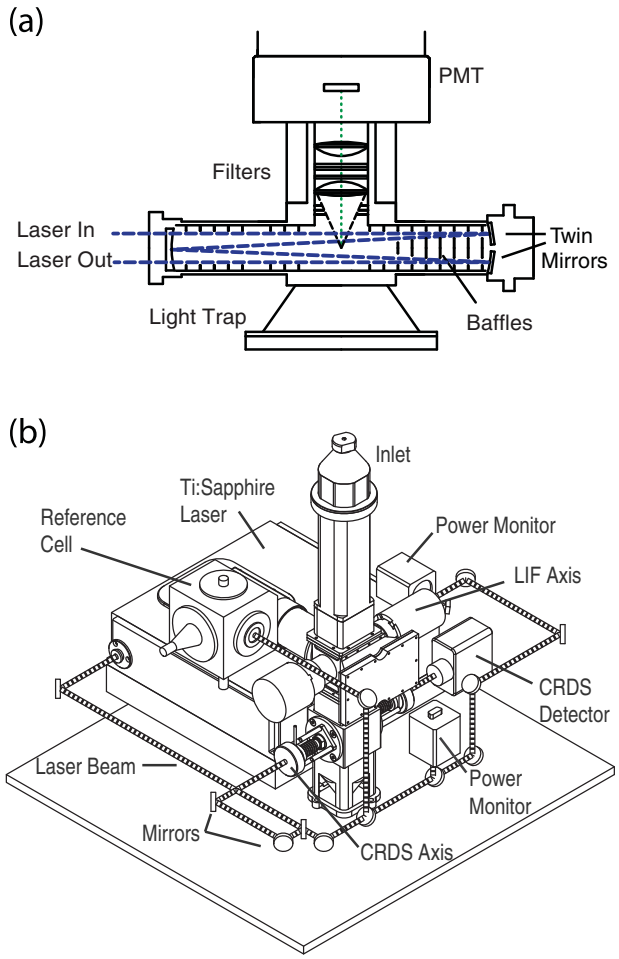

FIG. 6. A schematic of the optical systems. (a) A 32-pass White cell is used. Two lenses image the fluorescence from the central 1.5 cm of the White cell onto the photocathode of the PMT inside a refrigerated housing. Filters reject signal at the laser wavelength and provide high transmission at the observed fluorescence frequencies. Background noise and scattering are suppressed using optical baffles and a trapezoidal light trap across from the detector. Gas flow is in the direction perpendicular to the plane of the drawing. (b) The laser, optics, and detection axes are all configured on a 56 cm × 60 cm optical plate. The use of multiple vertical planes minimizes the footprint of the detection axis and enables each of the three detection axes (White cell, reference cell, CRDS cell) to be aligned independently.

D. Frequency reference cell

Changes in temperature, pressure, and humidity of air within the Ti:Sapphire cavity can result in shifts in the frequency of the laser on the order of the linewidth of the IO absorption features at 20 Torr. Rather than attempting to monitor the frequency of the laser directly, a reference cell in which IO is continuously generated is used to provide a stable metric of optical frequency. The frequency reference cell is a baffled, pressure-sealed, single-pass cell. The cell is filled to 20 Torr with a mixture of 20% CF_3I in ultra zero air in order to reproduce the line shapes anticipated in the White cell detection axis, which is operated at the same pressure. Current (~1A) is applied through a Nichrome filament to generate IO from the precursor molecules. While the chemical mechanism is not well defined, it is likely that I atoms are generated from CF_3I and react with oxygen to produce IO. Approximately 12-14 mW of the Ti:Sapphire laser light is directed into the frequency reference cell using a neutral density filter (Thorlabs NE01BA, Newton, NJ). A photomultiplier tube (Electro-Mechanical Research 541N-09, Sarasota, FL) in gated photon-counting mode is situated perpendicular to the axis of laser propagation to detect the laser-induced fluorescence signal at $\lambda > 500$ nm. A longpass interference filter (Semrock LP02-514RE-25, Rochester, NY) is used to reject scatter from the laser and other short-wave interferences. The concentration of IO in the cell is not quantified because the cell serves only as a frequency reference and does not play any further role in the calibration of the detection axis.

The leak rate of ambient air (<1 Torr per day) into the reference cell limits the amount of time it can operate prior to refilling (~10 days). As the pressure in the cell increases, the spectroscopic features broaden. Since the width of the reference cell peak is incorporated into an algorithm used to analyze data from the detection axis, the reference cell is refilled when pressures exceeds 28 Torr. The reference cell is equipped with solenoid valves to enable fast evacuation and recharging of the gas mixtures, limiting the system downtime to refill the reference cell to less than 10 min.

E. Optical design

A schematic of the optical design for the IO instrument is presented in Figure 6(b). The multilevel system is based on a standard optical breadboard with a 56 cm × 60 cm footprint. A series of lenses and turning mirrors condition the laser beam and direct it to the White cell, frequency reference cell, and a modular cavity ringdown detection axis used for calibrations. Two silicon photodiodes are used to monitor the laser power at 445 nm prior to and upon exit from the White cell as a metric for the alignment of the detection axis and to normalize the fluorescence signal. The compact design enables free-space coupling of the laser-beam, which is essential for maintaining a high beam quality for the multi-pass White cell and cavity ringdown detection systems.

F. Data acquisition

The data acquisition system for the instrument combines software written in LabVIEW, two 16-bit A/D cards (National Instruments PCI-6229, Austin, TX), and a custom-designed instrumental distribution panel. This data acquisition system is central to the operation of the instrument, controlling the commands sent by the software to hardware systems (e.g., sending voltages to the grating rotation stage, flow controllers, or laser shutter) and the acquisition of data coming from instrumental hardware (e.g., reading signals from PMTs, thermistors, photodiodes). Telemetry and signal data are written continuously at 1 Hz and 3 Hz respectively to a binary file.

The fluorescence signals from the White cell and reference cell are acquired using gated photon counting. The pulsed outputs from the PMTs are shaped with a pulse amplifier/discriminator and buffered with circuitry implemented on the instrumental distribution panel. The fluorescence signal must be collected during the laser pulse (30-40 ns) due to the short fluorescence lifetime of IO (<1 ns). The gated counting

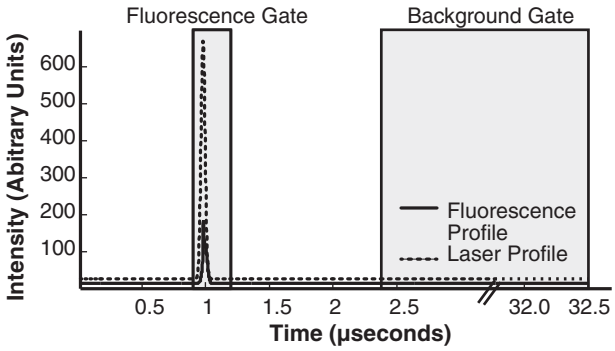

FIG. 7. Diagram of the gating scheme employed for photon counting. The trigger used to initiate gating occurs at time = 0 s. The measured fluorescence and laser profiles are shown. A fluorescence gate 300 ns long is used to capture the signal. A background gate 30 μs long detects continuous sources of background that occur after the fluorescence and short-lived interferences have subsided.

reduces the influence of solar scatter and other long-lived fluorescence interferences. A schematic of the gating scheme is presented in Figure 7. To generate the gate, the pulsed output from the Q-switch of the Nd:YAG is used as a trigger. A counter on the LabVIEW A/D card generates a 300 ns long gate delayed 1 μs from the rising edge of the Q-switch trigger. The "pause-trigger" functionality within LabVIEW is used to count the pulses from the PMT that arrive within the gate. For the White cell only, a second gate is used to collect the background signal that arises from solar scatter and dark counts. The background gate is 30 μs long and is delayed 2.4 μs relative to the rising edge of the Q-switch trigger. The gated counts are integrated over 330 ms (1650 laser pulses) before being recorded.

The software interface for the system is designed to operate autonomously for extended periods of time with no intervention. During normal operation, the system repeats a sequence of events to collect and record data. Figure 8 shows an example of the raw data collected during a typical acquisition sequence. First, the laser is physically shuttered so that dark counts can be recorded. The laser is then scanned from 445.00 nm to 445.05 nm across several rotational features in

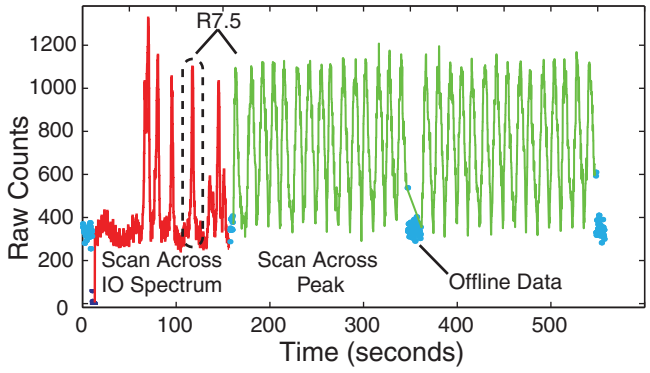

FIG. 8. The data acquisition sequence for the IO instrument. Off-resonance (cyan dots), and shuttered (black dots) measurements are collected. The laser is then tuned across several rotational lines in the IO spectrum (red line) and then is repeatedly tuned across the R7.5 rotational line (green). The R7.5 line is indicated within the black dashed rectangle in the IO spectrum and in green representing online data acquisition.

the IO spectrum. A peak-fitting algorithm is applied to the reference cell spectrum, and a logic-based process is used to determine the position of the R7.5 rotational line used for the measurement. The laser is tuned to the offline position prior to the peak, where background counts are recorded for 15 s. Online data are then acquired by tuning over approximately the top 50% of the R7.5 line in approximately 15 s. This online scan is repeated 15 times. After each online scan, a peak fitting analysis is performed to determine the peak center and adjust the scan range. Data are then acquired at the offline position to collect background counts for an additional 15 s. The online and offline acquisition sequence is repeated 15 times before reacquiring the IO spectrum. Status flags are assigned to each of these steps and recorded in the data stream to facilitate data analysis. In practice, this method of data acquisition is very reliable since the peak-fitting procedures can correct for any drift in laser frequency.

G. Deployment and operation

A mobile, weatherproof platform was developed for field deployment of the IO instrument. The instrument was designed to be compatible with a broad range of deployment conditions, particularly marine and polar environments where halogen chemistry is most active. An instrument deployed to these environments must be capable of withstanding temperature fluctuations, wind, precipitation, and corrosion. In its deployable package, the IO instrument is divided into two parts: (1) the sensor unit, which contains the inlet, laser, detection optics, and associated data acquisition electronics; and (2) the auxiliary unit, which contains the vacuum pump, ground fault circuit interrupters, uninterruptible power supply (UPS), and a chiller or water circulating pump. The elements in each unit are housed in a 1.3 m × 0.7 m × 0.6 m polypropylene copolymer case (Pelican Products Inc. 0550, Torrance, CA) customized with weather-tight plumbing and electrical connectors as well as the addition of brackets and vibration isolators to improve the stability of the optical alignment. The cases are fitted with chassis and large, low-pressure tires designed for movement over rugged terrain. The units can be configured not only with handles for movement by hand, but also have a ball hitch to enable towing with an all-terrain vehicle over longer distances.

Two different cooling strategies were designed for temperature control within the sensor unit. In both schemes, the sensor unit is cooled by a liquid loop that flows in parallel through two fan-circulated heat exchangers and the laser baseplate and diodes. Temperature sensors (E5CK-AA1-500, Omron, Kyoto, Japan) control the fans to prevent extreme fluctuations in operating temperature. In the first cooling scheme, a recirculating chiller (Thermo Neslab Inc. Coolflow CFT-75, Newington, NH) supplies the liquid loop with water of an approximately constant temperature (18 °C). This strategy was used in the field as well as in laboratory preparation of the instrument. The alternative strategy harnesses passive cooling by the ocean. A 30 cm × 20 cm aluminum heat exchanger is submerged in the ocean and a pump is used to circulate water through the heat exchanger and sensor box in a closed

loop. This approach has the advantage of requiring less energy and eliminating the need for refrigerants in sensitive environments. However, this strategy requires that the water pump be adequately sized to account for the vertical distance between the heat exchanger and the instrument, which depends on the operating environment.

The power requirements of the instrument are significant, ~ 4 kW peak power, with the majority of the power consumed by the scroll pump and chiller. The instrument is powered using 230V AC. In field environments without adequate local power supplies, a 10 kW diesel generator (Kubota Corporation GL 11000TM, Osaka, Japan) accompanies the instrument and can be situated approximately 100 feet away from the sensor unit. The generator is sized to ensure that the entire system can operate for more than 12 h without refueling.

IV. DATA ANALYSIS: CALCULATION OF THE MIXING RATIO OF IO

Post-acquisition processing of the data is required to convert the observed signals to atmospheric mixing ratios of IO. This section will describe the data processing steps including: normalizing the IO data, performing a nonlinear fit of the spectral feature, analysis and internal consistency tests to remove potential interferences, and tying the observed signal to IO concentrations by establishing an absolute calibration.

A. Calculating background-free, power-normalized signal

Continuous spectroscopic interferences and the impact of fluctuations in laser power must be removed from the observed fluorescence signal. First, the count rate measured during the background gate is subtracted from the count rate during the fluorescence gate. The observed signals from White cell and reference cell are then divided by the measured laser power (in Volts) to account for the linear dependence of fluorescence and other laser-induced interferences (e.g., laser scatter) on laser power. Finally, the mean of the offline data segments collected before and after each online peak scan is subtracted from the online peak scans.

B. Peak fitting

After the fluorescence signal of IO is isolated from the background, it is quantified using a peak fitting procedure. Since the laser is tuned across the R7.5 rotational line in the ro-vibronic spectrum, the online signal reflects the lineshape. For the specific conditions of this measurement, the lineshape is dictated by a combination of Lorentzian terms, i.e., natural broadening (HWHM = 2.33×10^{-4} nm) and pressure broadening (HWHM = 4.25×10^{-6} nm), and Gaussian terms, i.e., Doppler broadening (FWHM = 4.586×10^{-4} nm) and laser broadening (FWHM = 6.62×10^{-4} nm). While a Voigt profile is the best model for a lineshape that is a convolution of Gaussian and Lorentzian terms, the fitting procedure for a Voigt profile is computationally expensive. Since the data acquisition system narrows the range of wavelengths sampled to emphasize the center of the spectral line at the expense of the shoulders, fitting the line to a Gaussian function is a reasonable and computationally efficient approximation.

The first step in the fitting procedure is to perform a nonlinear least-squares fit of the reference cell data, which have high signal to noise ratios. The fits of the reference cell peaks show high R^2 values (>0.98) and no significant structure in the residuals, confirming that the Gaussian model is a good approximation for the observed line. The line center determined in the reference cell is then used to constrain the line center for the Gaussian fit of the White cell data, which typically have lower signal to noise. The quality of the fit is assessed using the goodness of fit parameter and the linewidth. These constraints are used to identify fitting errors that may result from the successful fitting of optical noise. The height of the peak derived from the fit is the proxy for the IO fluorescence signal, S_{IO}, in counts V^{-1} $s^{-1.}$

S_{IO} can be related to the mixing ratio of IO in the atmosphere $[IO]_{atm}$ with the following equation:

$$[IO]_{atm} = S_{IO}\left(\frac{1}{T_E\, C_{LIF}}\right), \tag{3}$$

where TE is the transmission efficiency (0.83 ± 0.04) determined from laboratory tests of the inlet, and C_{LIF} is an experimentally determined calibration factor (counts s^{-1} V^{-1} $pptv^{-1}$), which will be described in Sec. IV C.

C. Calibration

The fluorescence signal is related to a mixing ratio of IO by performing a standard addition experiment with calibrated amounts of IO. IO is generated in the laboratory by titrating known quantities of a certified standard of 9 nmol mol^{-1} CF_3I in N_2 (Scott-Marrin, Inc., Riverside, CA) with an excess of atomic oxygen. The CF_3I is diluted with a bulk flow of N_2 to maintain the overall flow rate and is introduced into the 32-pass LIF detection axis through a calibration assembly that is mounted on top of the instrumental inlet. Atomic oxygen is generated by passing a 0.6% mixture of O_2 in helium through a microwave discharge (Scintillonics Inc. HV15A, Fort Collins, CO). A custom designed quartz loop injector (James Glass, Hanover, MA) is used to introduce atomic oxygen to the center of the flow approximately 4 cm downstream of the pinhole inlet where it mixes with the CF_3I/N_2. IO is produced from the following reaction with a known yield of 83% ± 11%:[73]

$$CF_3I + O \rightarrow IO + CF_3. \tag{4}$$

CF_3I is added by standard addition with a constant flow rate of O_2. The experiment is then repeated over a range of O_2 flow rates to determine the conditions under which the production of IO is limited by available CF_3I rather than atomic oxygen. Figure 9(a) shows the fluorescence signal as a function of O_2 flow rate with a constant amount of CF_3I added. The plateau in fluorescence signal at higher flow rates of O_2 that is observed suggests that O is present in excess under those conditions. The results of a standard addition experiment conducted with 2 different O_2 flow rates are depicted in Figure 9(b).

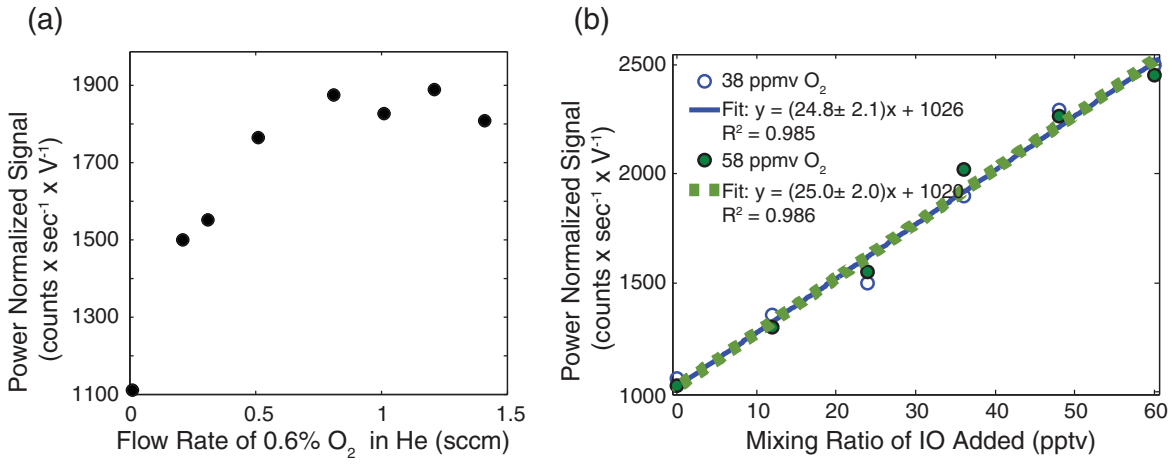

FIG. 9. Results from a typical chemical titration calibration. This experiment was performed at the Shoals Marine Laboratory on August 18th, 2011. (a) A standard addition experiment is performed at a variety of O_2 flow rates, shown here for a constant 400 sccm flow of 9 ppbv CF_3I in N_2. An excess of atomic oxygen indicated by the plateau in signal change at higher O_2 flow rates. (b) A standard addition of IO is performed with a constant concentration of added O_2. The slope of the linear fit of the standard addition data is the calibration factor.

The concentration of IO measured at the detection axis is determined from the concentration of added CF_3I, and the yield of Reaction 4 (83% ± 11%). A kinetic model is used to account for the chemical losses that occur between the time of production of IO and its detection. The dominant chemical loss pathways and associated rate constants[74] in units of cm^3 mol^{-1} s^{-1} are:

$$IO + IO \rightarrow OIO + I$$
$$k = .44 \times \left(1.5 \times 10^{-11}\right) \times exp\left(500/T\right), \qquad (5)$$

$$IO + IO \rightarrow 2I + O_2$$
$$k = .56 \times \left(1.5 \times 10^{-11}\right) \times exp\left(500/T\right), \qquad (6)$$

$$IO + O \rightarrow I + O_2 \qquad k = 1.2 \times 10^{-10}. \qquad (7)$$

Since the calibration is performed in excess atomic oxygen, the losses due to Reaction 7 are significant. Therefore, a direct measurement of the concentration of atomic oxygen is required to quantify chemical losses in the kinetic model.

The concentration of atomic oxygen is measured by incorporating an absorption axis directly downstream of the position where atomic oxygen atoms are introduced into the flow. The light source is an atomic oxygen lamp, fabricated in our laboratory with a $KMnO_4$ source. The absorption of the oxygen line ($^3S_1 \leftarrow {}^3P_0$) at 130.6 nm is monitored with a 0.2 meter vacuum monochromator (Acton Research Corporation VM-502, Acton, MA). Using the Beer-Lambert law, the concentration of atomic oxygen is calculated from the measured transmittance, the absorption cross-section ($1.64 \times 10^{-13} \pm 0.36 \times 10^{-13}$ cm^2 mol^{-1}[75]), and the pathlength (5.08 cm). The yield of atomic oxygen relative to the molecular oxygen added is low (<5%), which is likely due to a combination of inefficient production of O by the discharge and large losses within the quartz loop injector. The concentration of O is incorporated into the chemical loss model to correct for the losses of IO that occur within the duct. A 22% uncertainty in calculated concentrations of O is derived from uncertainties in the absorption cross section (20%) and absorption measurement (11%). Above a threshold level of 25 ppmv of added O_2, the yield of IO produced did not show significant dependence on additional O_2 for the conditions of the calibrations performed in this work. Only calibration data performed at O_2 mixing ratios greater than 35 ppmv and less than 60 ppmv were used in sensitivity calculations to ensure that small variations in the concentration of atomic oxygen produced would not affect the result.

The sensitivity of the LIF detection is determined from the slope of a least squares regression of the fluorescence signal as a function of the IO mixing ratio introduced into the system (e.g., Figure 9(b)). The observed linearity in LIF signal observed as a function of IO mixing ratio implies that the absorption step is not saturated and the PMT is operating in a linear range over atmospherically relevant IO concentrations. The sensitivity of the LIF detection is reported as a calibration factor, C_{LIF}, in units of counts s^{-1}(pptv IO)$^{-1}$ V^{-1} at 20 Torr. The standard addition experiments in Figure 9 were performed during a field deployment of the IO instrument. Two different concentrations of added O_2 yielded C_{LIF} values from the fitting procedure of 25.0 ± 2.0 and 24.8 ± 2.1 counts s^{-1} (pptv IO) $^{-1}$ V^{-1}.

The instrument has also been designed to incorporate a secondary method of calibration by cavity ringdown spectroscopy (CRDS), which has orthogonal sources of uncertainty relative to chemical titration. A modular CRDS axis is configured downstream of the LIF detection axis so that calibration can be tied to the absolute absorption cross section.[54,76] This method is less appropriate for field calibrations. Given the pathlength of the cell (22 cm) and mirror reflectivity (currently 99.95% at 445 nm), concentrations of IO above 8×10^8 molecules of IO per cm^3 (~1 ppbv at 20 Torr) are required for CRDS detection. The introduction of high concentrations of IO precursors can contaminate the surfaces within the instrument and reduce the reflectivity

of the mirrors. While the CRDS calibration was not implemented in the field, calibrations were performed previously with higher reflectivity (>99.99%) mirrors (Los Gatos Research—no longer available, Mountain View, CA) in the laboratory. Calibration factors determined with CRDS and LIF in the laboratory agree to within less than 10%, well within the uncertainty of the individual methods.

D. Uncertainty

Given the relatively low concentrations of IO anticipated in the atmosphere, a thorough analysis of the uncertainty of the IO measurement is required. To quantify the reproducibility of the peak fitting technique used to determine the peak height, a statistical bootstrap analysis of the fitting procedure was conducted to estimate the variance. This analysis is detailed in Sec. S2 of the supplementary material.[69] The calculation of the yield of IO from CF_3I (11%), the laser power measurement (3%), and the fitting procedure (8%) all contribute to an overall 2σ measurement uncertainty of 14%. The end-to-end estimate of measurement uncertainty for the instrument is 21% (2σ), resulting from the 14% and 16% uncertainties in the determination of C_{LIF} and TE, respectively.

The uncertainty at low concentrations of IO is dominated by the peak fitting since the other sources of uncertainty are relative and scale with concentration. The bootstrap analysis revealed that the 1σ uncertainty associated with the fitting procedure is 0.2 pptv for each individual peak fit. Four peak fits are averaged for each reported 1-min data point, so the 1σ uncertainty, which scales with $\frac{1}{\sqrt{N}}$, where N = 4, is 0.1 pptv for the minute-averaged measurement. The limit of detection, defined as the threshold concentration of IO where the signal to noise ratio equals 3, is 0.3 pptv in 1 min.

It should be noted that the excitation rate of IO depends on temperature. The use of a narrow-linewidth excitation source in this experiment enables the excitation of electrons from a single rotational level ($v'' = 0$, $J'' = 7.5$) in the $X^2\Pi_{3/2}$ state of IO. The normalized population density of the rotational state will vary as a function of temperature. The calibrations and measurements presented in this work occurred within a relatively narrow temperature range since the detection axis temperature was tightly regulated. However, corrections to the calibration using ambient temperature observations would be required for airborne measurements. The relative population densities can be calculated directly using spectroscopic constants and measurements of temperature.[59]

V. FIELD VALIDATION

A. Site description

The prototype instrument was deployed to Shoals Marine Lab (SML) on Appledore Island, ME, a marine science facility affiliated with Cornell University and the University of New Hampshire. Appledore Island (42°58′ N, 70°37′ W), approximately 10 km from Portsmouth, NH, is the largest island within an archipelago known as the Isles of Shoals. This site was chosen for the validation of the Harvard IO instrument because Stutz *et al.*[40] measured IO by LP and MAX-DOAS there previously as a part of the Chemistry of Halogens at the Isles of Shoals (CHAiOS) field campaign in 2004. The light path of the LP-DOAS instrument extended from Appledore Island to neighboring White Island (Figure 10) and ranged from 15 to 35 m above the ocean surface. Reactive iodine species (IO and OIO) were measured by the LP-DOAS instrument on 19 of 23 days, with a maximum mixing ratio of 4 pptv for IO.

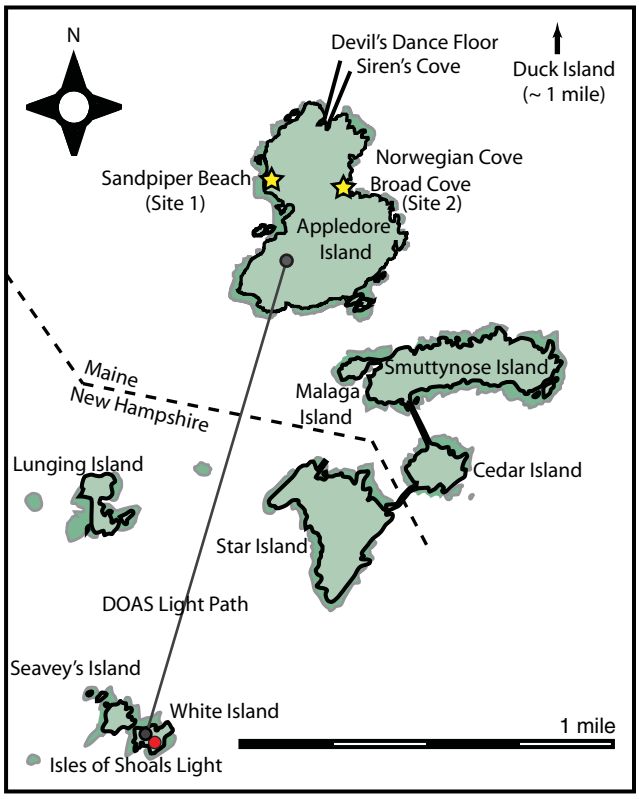

FIG. 10. A map of the Isles of Shoals. The light path of the long path DOAS instrument deployed in 2004 is indicated spanning from Appledore Island to White Island. LIF measurement sites are indicated (yellow stars). From August 17th to August 25th, 2011 measurements were made at site 1. From August 31st to September 5th, measurements were made at site 2. Kelp stands had been observed near Siren's Cove, Devil's Dance Floor, and Norwegian Cove in previous years. (Map adapted with permission from W. E. Beamis, Shoals Marine Laboratory.)

The Harvard IO instrument was deployed for validation from August 17th to September 5th, 2011. Data were not collected on August 20 due to heavy rains or during the period from August 26th to August 30th due to the onset of Hurricane Irene. Observations were made from two different measurement sites on opposite sides of the island, as depicted in Figure 10. From August 17th to August 25th, observations were made from the western shoreline of the island near Sand Piper Beach (site 1). This relatively sheltered site was selected due to a combination of prevailing onshore winds and the accessibility of terrain near the high-tide line. Observations from August 31st to September 3rd were carried out on the eastern shoreline of the island, near Broad Cove (site 2). Broad Cove has sheer walls and is significantly more exposed than Sandpiper Beach.

Laminariales (kelp) considered largely responsible for the tidal signatures observed in emissions at Mace Head,

Ireland and Roscoff, France, were not observed to be actively growing at either site.[10,13,28] However, abundant *Saccharina latissima* and limited quantities of *Laminaria digitata* washed ashore in the days after Hurricane Irene near Broad Cove. Individuals familiar with the ecology of the island indicated that kelp stands grow most frequently on the northern edge of the island near Siren's Cove as well as in the area surrounding Norwegian Cove.[77] These northerly sites were inaccessible for sampling due to densely wooded terrain.

B. Field performance

The sensitivity of the measurement is directly impacted by changes in laser power and fluctuations in the alignment of the White cell. Laser power decreased by ~40% early in the deployment. Humidity changes within the sensor box and resulting condensation onto optics within the laser was likely the cause of the decreased power. To prevent condensation, the sensor unit, and the laser specifically, were aggressively purged with nitrogen and packets of a silica-based drying agent were used to keep the relative humidity below 25%. Dry operating conditions reversed laser power losses and increased the laser stability for the remainder of the deployment. The practice of normalizing signal by observed laser power mitigates the impact of fluctuations in power on the measurement. During the field deployment, the optical system was remarkably stable. No realignment of the White cell was required after leaving the laboratory. There were no rapid changes in transmission and the overall change in alignment, even after transporting the instrument, was less than 10% throughout the deployment. The average transmission of the laser through the White cell during the deployment was 87%. Despite very high transmission through the cell, elevated levels of background counts were observed during the fluorescence gate. In order to avoid nonlinearity in photon counting by the PMT, only a fraction of the total laser light was coupled into the cell, typically on the order of 20-25 mW. Field calibrations were performed to assess the overall sensitivity of the instrument. The field calibrations agreed to within 5% with calibrations performed in the laboratory.

C. Results

The observed mixing ratios of IO during the deployment to Shoals Marine Laboratory are presented in Figure 11. It should be noted that on DOY 231, replacing the anodized aluminum inlet with a version optically blackened with a copper oxide coating (Ebonol-C) significantly reduced the solar scatter detected by the PMT. While the inlet does not account for all scatter within the data, it significantly reduced background optical counts and reduced errors in the peak-fitting algorithm used to determine the IO mixing ratio.

Minute-averaged mixing ratios ranged from below the instrumental detection limit (0.3 pptv) up to 10 pptv. The maximum IO signal corresponded to daytime low tide events, which is consistent with observations of IO at coastal sites in Europe.[7–10,34,48] This tidal dependence is attributed to the exposure of macroalgae to oxidative stress, resulting in the release of molecular iodine and photo-labile iodocarbons.[78] Figure 12(a) shows the IO signal as a function of time of day. A diurnal trend is apparent in the IO observations with the lowest mixing ratios observed at night and generally higher mixing ratios with significantly higher variability during the day. IO was measured during 4 complete nights in the observation period. The majority of measurements were at or below the detection limit of the instrument, but IO was measured above the detection limit on DOY 233/234 with a mixing ratio of 1.4 pptv. These observations took place immediately following Hurricane Irene, when there was generally more scatter in the observations. The positive detection may have arisen from large quantities of macroalgae that had been washed ashore above the high tide line near the instrument. The only known pathway for IO production in the absence of photolysis is the reaction of I_2 with NO_3.[79,80] Figure 12(b) shows the dependence of IO on tidal exposure. Tidal exposure was calculated by taking the inverse of tidal height and linearly mapping it onto a scale from 0 to 1, where 1 represents the lowest tide observed during the observation period. While maximal mixing ratios of IO were observed during low tide events (Figure 11), the overall correlation between IO and tidal height is low ($R = 0.01$).

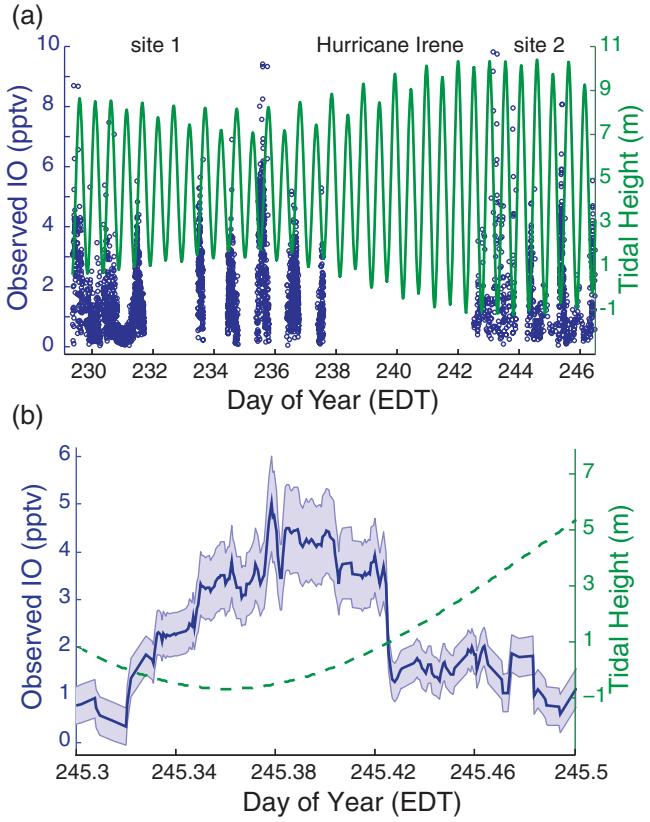

FIG. 11. Timeseries of observed IO mixing ratios. (a) Timeseries of IO mixing ratio (solid blue circles) and tidal height (green line) observed at the Shoals Marine Lab during late August and early September 2011. (b) IO (solid blue line) with 2σ uncertainty (light blue envelope) observed at site 2 on September 1st (DOY 245).

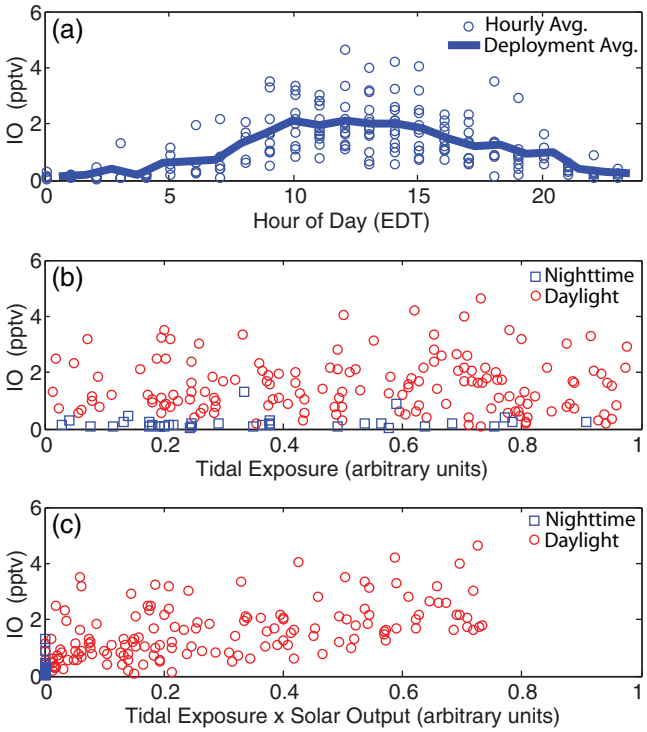

FIG. 12. Dependence of IO on time of day and tidal height. (a) Binned hourly averaged IO signal as a function of time of day (blue circles) shows a clear diurnal dependence. (b) IO signal as a function tidal height shows no correlation (R = 0.01). (c) IO is plotted as a function of the product of tidal exposure and solar output (R = 0.65). Tidal exposure and solar output were mapped onto a scale from 0 to 1 such that a value of 1 on the plot represents maximal solar output and the lowest tides observed during the observation period.

D. Discussion

1. Comparison with other in situ observations

Maximum mixing ratios of IO observed at Shoals Marine Laboratory (~10 pptv) were not as large as those observed by *in situ* measurements in European coastal sites (~30 pptv) with large laminaria populations,[10,48] but the observations show similar tidal dependence. A major difference between European measurements and those in New England is the relationship between the tides and solar output. In Mace Head and Roscoff, the lowest spring tides occurred close to solar noon. At the Isles of Shoals, the low spring tides occurred at dawn and dusk. The observations of IO in coastal regions are dependent on 2 major factors: (1) the exposure of macroalgae to oxidative stress and (2) the generation of IO from iodine-containing precursors, which is governed primarily by photolysis. Accordingly, midday spring tides that expose macroalgae that efficiently emit iodine provide optimal conditions for the production of IO. At the Isles of Shoals, photolysis rates were low during the most extreme low tide events, reducing the likelihood of observing high concentrations of reactive iodine based on currently understood mechanisms. The product of tidal exposure (described in Sec. V C) and solar output provides a useful metric for the constraint on the production of IO. The photolysis rate constant for Cl_2, as calculated from the National Center for Atmospheric Research Tropospheric Ultraviolet and Visible Radiation (TUV) model,[81] is used as the metric of solar output and is normalized to a scale ranging from 0 to 1. This metric of solar exposure is only qualitative because there are differences in the photolysis frequencies of Cl_2 and I_2, and the model does not account for deviation from clear-sky conditions. The correlation (R = 0.65) between IO and the product of solar output and tidal exposure is significantly higher than for tidal height alone.

Differences in local ecology may also account for the lower mixing ratios and the low correlation with tidal height reported here relative to the European sites. At both Mace Head and Roscoff, there are large laminaria populations in the intertidal range, including *Laminaria digitata,* which is a particularly potent emitter of iodine when it is exposed at the lowest tides. In contrast, laminaria populations are declining in the Gulf of Maine with losses of as much as 95% seen in some kelp beds over a 20 year period.[82] No kelp stands were observed growing in the intertidal range of Appledore Island during the sampling period. Testing of the macroalgae samples collected at the site (see Sec. S3 of the supplementary material[69]) revealed that the strongest emissions from locally growing species came from *Fucus vesiculosus*, which was abundant in the intertidal range. If *Fucus vesiculosus* was responsible for the emissions, it provides a potential explanation the low correlation of IO emissions with tidal height, since it is fully exposed during larger portions of the tidal range and emits I_2 for a longer duration[83] after it is initially exposed relative to *Laminaria digitata.*

2. Comparison with LP DOAS observations at Appledore Island

The observations reported here, specifically the magnitudes of IO measured, agree well with the LP-DOAS observations at the Isles of Shoals.[40] One difference between these observations and the DOAS measurements is that the latter indicated no tidal signature. This discrepancy may be due to the combination of inherent differences in spatial coverage and the generally weak tidal dependence described previously. Only a small fraction of the LP-DOAS light path is in the intertidal range. As a result, the LP-DOAS measurement may be more sensitive to IO produced from the photolysis of longer-lived precursors transported from the intertidal regions or from emissions over the open ocean, which are not well understood. While the lack of coordinated measurements in this study limits the extent of the analysis of this dataset, the measurements at SML validate the field readiness of the Harvard IO instrument and provide a first *in situ* point measurement of IO in North America.

VI. CONCLUSIONS AND FUTURE WORK

There are several requirements of an IO instrument suitable for improving scientific understanding. First, the instrument must be highly sensitive since mixing ratios of IO are frequently below 5 pptv in the boundary layer. To achieve high precision and accuracy, the instrument must be free of interferences and be well calibrated for potential losses of IO given its reactivity. Second, the instrument must be capable of probing changes in the concentration of IO in space and time.

Mobility and fast time response are essential for measuring concentrations of IO in a range of environments and altitudes.

We have built and successfully deployed an instrument to measure IO *in situ* by laser-induced fluorescence that meets these criteria. Data from a field deployment to the Shoals Marine Laboratory demonstrated the sub-pptv sensitivity of the instrument under field conditions. By tuning across the spectroscopic line and implementing a reference cell, the potential for interference is reduced and fast time response is retained. The multipass detection scheme yielded a 0.3 pptv limit of detection (3σ) in 1 min. Further, we have demonstrated that the instrument, which has a compact, mobile, and weatherproof design, is adequately stable for deployment on a range of platforms, including aircraft. While the Harvard IO instrument is, to our knowledge, the most sensitive implementation of an *in situ* measurement reported, several improvements could further increase the sensitivity of the instrument and reduce the detection limit. Reductions in chamber scatter achieved with improved optical coatings within the White cell will enable a greater fraction of the laser power to be used for detection yielding increases in sensitivity.

The IO instrument has been designed to be fundamentally compatible with aircraft based deployment for broader tropospheric and stratospheric coverage. While the instrument could be deployed on its own, a more potent experiment would be to combine the IO system with the existing BrO, ClO, and NO_2 aircraft instruments built by our laboratory. Integrating the IO instrument with the BrO and ClO detection axes would provide significant power and weight savings since the measurements would share several components (i.e., inlet and vacuum pump). The merging of these instruments would create a payload uniquely capable of probing the halogen budget throughout the atmosphere and resolving open questions about the role of IO throughout the free troposphere and lower stratosphere.

ACKNOWLEDGMENTS

The authors wish to thank Norton Allen, Joe Demusz, Mike Greenberg, Matt Knight, Terry Martin, Danny Spillane, Ed Thomspon, and Chris Tuozzolo for engineering support. M.T. wishes to thank the staff of the Shoals Marine Laboratory and Charles Praska for logistical assistance and Steven Wofsy and Roisín Commane for technical advice. This work was supported by the National Science Foundation (Award No.: 0733875).

[1]J. B. Burkholder, J. Curtius, A. R. Ravishankara, and E. R. Lovejoy, Atmos. Chem. Phys. **4**, 19–34 (2004).
[2]R. W. Saunders and J. M. C. Plane, Environ. Chem. **2**(4), 299–303 (2005).
[3]R. W. Saunders and J. M. C. Plane, J. Aerosol. Sci. **37**(12), 1737–1749 (2006).
[4]R. W. Saunders, R. Kumar, J. C. Gómez Martín, A. S. Mahajan, B. J. Murray, and J. M. C. Plane, Z. Phys. Chem. **224**(7-8), 1095–1117 (2010).
[5]J. D. Whitehead, G. B. McFiggans, M. W. Gallagher, and M. J. Flynn, Geophys. Res. Lett. **36**, L04806, doi:10.1029/2008gl035969 (2009).
[6]A. S. Mahajan, H. Oetjen, A. Saiz-Lopez, J. D. Lee, G. B. McFiggans, and J. M. C. Plane, Geophys. Res. Lett. **36**(16), L16803, doi:10.1029/2009gl038018 (2009).
[7]R. Wada, J. M. Beames, and A. J. Orr-Ewing, J. Atmos. Chem. **58**(1), 69–87 (2007).
[8]L. K. Whalley, K. L. Furneaux, T. Gravestock, H. M. Atkinson, C. S. E. Bale, T. Ingham, W. J. Bloss, and D. E. Heard, J. Atmos. Chem. **58**(1), 19–39 (2007).
[9]K. Seitz, J. Buxmann, D. Pohler, T. Sommer, J. Tschritter, T. Neary, C. O'Dowd, and U. Platt, Atmos. Chem. Phys. **10**(5), 2117–2128 (2010).
[10]K. L. Furneaux, L. K. Whalley, D. E. Heard, H. M. Atkinson, W. J. Bloss, M. J. Flynn, M. W. Gallagher, T. Ingham, L. Kramer, J. D. Lee, R. Leigh, G. B. McFiggans, A. S. Mahajan, P. S. Monks, H. Oetjen, J. M. C. Plane, and J. D. Whitehead, Atmos. Chem. Phys. **10**(8), 3645–3663 (2010).
[11]R. J. Huang, K. Seitz, T. Neary, C. D. O'Dowd, U. Platt, and T. Hoffmann, Geophys. Res. Lett. **37**, L03803, doi:10.1029/2009gl041467 (2010).
[12]J. M. Mäkelä, T. Hoffmann, C. Holzke, M. Väkevä, T. Suni, T. Mattila, P. P. Aalto, U. Tapper, E. I. Kauppinen, and C. D. O'Dowd, J. Geophys. Res., [Atmos.] **107**(D19), 8110, doi:10.1029/2001JD000580 (2002).
[13]A. Saiz-Lopez and J. M. C. Plane, Geophys. Res. Lett. **31**(4), L04112, doi:10.1029/2003gl019215 (2004).
[14]A. Saiz-Lopez, J. A. Shillito, H. Coe, and J. M. C. Plane, Atmo. Chem. Phys. **6**, 1513–1528 (2006).
[15]C. D. O'Dowd, J. L. Jimenez, R. Bahreini, R. C. Flagan, J. H. Seinfeld, K. Hameri, L. Pirjola, M. Kulmala, S. G. Jennings, and T. Hoffman, Nature (London) **417**, 632–634 (2002).
[16]J. G. Calvert and S. E. Lindberg, Atmos. Environ. **38**(30), 5105–5116 (2004).
[17]M. E. Goodsite, J. M. C. Plane, and H. Skov, Environ. Sci. Technol. **38**, 1772–1776 (2004).
[18]W. L. Chameides and D. D. Davis, J. Geophys. Res., C: Oceans Atmos. **85**(Nc12), 7383–7398 (1980).
[19]J. G. Calvert and S. E. Lindberg, Atmos. Environ. **38**(30), 5087–5104 (2004).
[20]S. Solomon, R. R. Garcia, and A. R. Ravishankara, J. Geophys. Res., [Atmos.] **99**(D10), 20491–20499, doi:10.1029/94JD02028 (1994).
[21]R. Vogt, R. Sander, R. V. Glasow, and P. J. Crutzen, J. Atmos. Chem. **32**, 375–379 (1999).
[22]W. J. Bloss, J. D. Lee, G. P. Johnson, R. Sommariva, D. E. Heard, A. Saiz-Lopez, J. M. C. Plane, G. McFiggans, H. Coe, M. Flynn, P. Williams, A. R. Rickard, and Z. L. Fleming, Geophys. Res. Lett. **32**(6), L06814, doi:10.1029/2004gl022084 (2005).
[23]K. A. Read, A. S. Mahajan, L. J. Carpenter, M. J. Evans, B. V. E. Faria, D. E. Heard, J. R. Hopkins, J. D. Lee, S. J. Moller, A. C. Lewis, L. Mendes, J. B. McQuaid, H. Oetjen, A. Saiz-Lopez, M. J. Pilling, and J. M. C. Plane, Nature (London) **453**(7199), 1232–1235 (2008).
[24]A. Saiz-Lopez, J. M. Plane, A. R. Baker, L. J. Carpenter, R. von Glasow, J. C. Gómez Martín, G. McFiggans, and R. W. Saunders, Chem. Rev. **112**(3), 1773–1804 (2012).
[25]C. E. Jones, K. E. Hornsby, R. Sommariva, R. M. Dunk, R. Von Glasow, G. McFiggans, and L. J. Carpenter, Geophys. Res. Lett. **37**, L18804, doi:10.1029/2010gl043990 (2010).
[26]L. J. Carpenter, W. T. Sturges, S. A. Penkett, P. S. Liss, B. Alicke, K. Hebestreit, and U. Platt, J Geophys. Res.: Atmos. **104**,(D1), 1679–1689 (1999).
[27]L. J. Carpenter, P. S. Liss and S. A. Penkett, J. Geophys. Res.: Atmos. **108**(D9), 4256, doi:10.1029/2002jd002769 (2003).
[28]G. McFiggans, H. Coe, R. Burgess, J. Allan, M. Cubison, M. R. Alfarra, R. Saunders, A. Saiz-Lopez, J. M. C. Plane, D. J. Wevill, L. J. Carpenter, A. R. Rickard, and P. S. Monks, Atmos. Chem. Phys. **4**, 701–713 (2004).
[29]S. Klick and K. Abrahamsson, J. Geophys. Res.: Oceans **97**(C8), 12683–12687 (1992).
[30]M. Pedersen, J. Collen, K. Abrahamsson, and A. Ekdahl, Sci. Mar. **60**, 257–263 (1996).
[31]L. J. Carpenter, G. Malin, P. S. Liss, and F. C. Küpper, Global Biogeochem. Cy. **14**(4), 1191–1204 (2000).
[32]L. J. Carpenter, S. M. MacDonald, M. D. Shaw, R. Kumar, R. W. Saunders, R. Parthipan, J. Wilson, and J. M. C. Plane, Nat. Geosci. **6**(2), 108–111 (2013).
[33]B. Alicke, K. Hebestreit, J. Stutz, and U. Platt, Nature (London) **397**(6720), 572–573 (1999).
[34]B. J. Allan, G. McFiggans, J. M. C. Plane, and H. Coe, J. Geophys. Res., [Atmos.] **105**(D11), 14363–14369, doi:10.1029/1999JD901188 (2000).
[35]A. Saiz-Lopez, J. F. Lamarque, D. E. Kinnison, S. Tilmes, C. Ordonez, J. J. Orlando, A. J. Conley, J. M. C. Plane, A. S. Mahajan, G. S. Santos, E. L. Atlas, D. R. Blake, S. P. Sander, S. Schauffler, A. M. Thompson, and G. Brasseur, Atmos. Chem. Phys. **12**(9), 3939–3949 (2012).
[36]J. Zingler and U. Platt, J. Geophys. Res., [Atmos.] **110**(D7), D07307, doi:10.1029/2004JD004993 (2005).

[37]A. Saiz-Lopez, A. S. Mahajan, R. A. Salmon, S. J. B. Bauguitte, A. E. Jones, H. K. Roscoe, and J. M. C. Plane, Science **317**(5836), 348–351 (2007).
[38]A. S. Mahajan, M. Shaw, H. Oetjen, K. E. Hornsby, L. J. Carpenter, L. Kaleschke, X. Tian-Kunze, J. D. Lee, S. J. Moller, P. Edwards, R. Commane, T. Ingham, D. E. Heard, and J. M. C. Plane, J. Geophys. Res.: Atmos **115**, D20303, doi:10.1029/2009jd013665 (2010).
[39]C. Peters, S. Pechtl, J. Stutz, K. Hebestreit, G. Hönninger, K. G. Heumann, A. Schwarz, J. Winterlik, and U. Platt, Atmos. Chem. Phys. **5**, 3357–3375 (2005).
[40]J. Stutz, O. Pikelnaya, S. C. Hurlock, S. Trick, S. Pechtl, and R. von Glasow, Geophys. Res. Lett. **34**(22), L22816, doi:10.1029/2007gl031332 (2007).
[41]B. J. Allan, J. M. C. Plane, and G. McFiggans, Geophys. Res. Lett. **28**(10), 1945–1948, doi:10.1029/2000GL012468 (2001).
[42]J. C. Gómez Martín, A. S. Mahajan, T. D. Hay, C. Prados-Roman, C. Ordonez, S. M. MacDonald, J. M. C. Plane, M. Sorribas, M. Gil, J. F. P. Mora, M. V. A. Reyes, D. E. Oram, E. Leedham, and A. Saiz-Lopez, J. Geophys. Res., [Atmos.] **118**(2), 887–904, doi:10.1002/jgrd.50132 (2013).
[43]K. Großmann, U. Frieß, E. Peters, F. Wittrock, J. Lampel, S. Yilmaz, J. Tschritter, R. Sommariva, R. von Glasow, B. Quack, K. Krüger, K. Pfeilsticker, and U. Platt, Atmos. Chem. Phys. **13**, 3363–3378 (2013).
[44]U. Frieß, T. Wagner, I. Pundt, K. Pfeilsticker, and U. Platt, Geophys. Res. Lett. **28**(10), 1941–1944, doi:10.1029/2000GL012784 (2001).
[45]B. Dix, S. Baidar, J. F. Bresch, S. R. Hall, K. S. Schmidt, S. Wang, and R. Volkamer, Proc. Natl. Acad. Sci. U.S.A. **110**(6), 2035–2040 (2013).
[46]F. Wittrock, R. Muller, A. Richter, H. Bovensmann, and J. P. Burrows, Geophys. Res. Lett. **27**(10), 1471–1474, doi:10.1029/1999GL011146 (2000).
[47]O. Puentedura, M. Gil, A. Saiz-Lopez, T. Hay, M. Navarro-Comas, A. Gómez-Pelaez, E. Cuevas, J. Iglesias, and L. Gomez, Atmos. Chem. Phys. **12**, 4909–4921 (2012).
[48]R. Commane, K. Seitz, C. S. E. Bale, W. J. Bloss, J. Buxmann, T. Ingham, U. Platt, D. Pöhler, and D. E. Heard, Atmos. Chem. Phys. **11**(13), 6721–6733 (2011).
[49]A. S. Mahajan, J. C. Gómez Martín, T. D. Hay, S. J. Royer, S. Yvon-Lewis, Y. Liu, L. Hu, C. Prados-Roman, C. Ordonez, J. M. C. Plane, and A. Saiz-Lopez, Atmos. Chem. Phys. **12**(23), 11609–11617 (2012).
[50]A. Saiz-Lopez, K. Chance, X. Liu and T. P. Kurosu, Geophys. Res. Lett. **34**(L12), 812–817 (2007).
[51]A. Schönhardt, A. Richter, F. Wittrock, H. Kirk, H. Oetjen, H. K. Roscoe, and J. P. Burrows, Atmos. Chem. Phys. **8**(3), 637–653 (2008).
[52]N. J. Blake, D. R. Blake, T. Y. Chen, J. E. Collins, G. W. Sachse, B. E. Anderson, and F. S. Rowland, J. Geophys. Res., [Atmos.] **102**(D23), 28315–28331, doi:10.1029/97JD02538 (1997).
[53]N. Bell, L. Hsu, D. J. Jacob, M. G. Schultz, D. R. Blake, J. H. Butler, D. B. King, J. M. Lobert, and E. Maier-Reimer, J. Geophys. Res., [Atmos.] **107**(D17), 4340, doi:10.1029/2001JD001151 (2002).
[54]P. O. Wennberg, J. W. Brault, T. F. Hanisco, R. J. Salawitch, and G. H. Mount, J. Geophys. Res., [Atmos.] **102**(D7), 8887–8898, doi:10.1029/96JD03712 (1997).
[55]I. Pundt, J. P. Pommereau, C. Phillips, and E. Lateltin, J. Atmos. Chem. **30**(1), 173–185 (1998).
[56]H. Bösch, C. Camy-Peyret, M. P. Chipperfield, R. Fitzenberger, H. Harder, U. Platt, and K. Pfeilsticker, J. Geophys. Res., [Atmos.] **108**(D15), 4455, doi:10.1029/2002JD003078 (2003).
[57]A. Butz, H. Bösch, C. Camy-Peyret, M. P. Chipperfield, M. Dorf, S. Kreycy, L. Kritten, C. Prados-Roman, J. Schwarzle, and K. Pfeilsticker, Atmos. Chem. Phys. **9**(18), 7229–7242 (2009).
[58]R. M. Stimpfle and J. G. Anderson, Geophys. Res. Lett. **15**(13), 1503–1506, doi:10.1029/GL015i013p01503 (1988).
[59]P. O. Wennberg, R. C. Cohen, N. L. Hazen, L. B. Lapson, N. T. Allen, T. F. Hanisco, J. F. Oliver, N. W. Lanham, J. N. Demusz, and J. G. Anderson, Rev. Sci. Instrum. **65**(6), 1858–1876 (1994).
[60]K. K. Perkins, T. F. Hanisco, R. C. Cohen, L. C. Koch, R. M. Stimpfle, P. B. Voss, G. P. Bonne, E. J. Lanzendorf, J. G. Anderson, P. O. Wennberg, R. S. Gao, L. A. Del Negro, R. J. Salawitch, C. T. McElroy, E. J. Hintsa, M. Loewenstein, and T. P. Bui, J. Phys. Chem. A **105**(9), 1521–1534 (2001).
[61]J. M. St Clair, T. F. Hanisco, E. M. Weinstock, E. J. Moyer, D. S. Sayres, F. N. Keutsch, J. H. Kroll, J. N. Demusz, N. T. Allen, J. B. Smith, J. R. Spackman, and J. G. Anderson, Rev. Sci. Instrum. **79**(6), 064101 (2008).
[62]A. A. Turnipseed, M. K. Giles, J. B. Burkholder, and A. R. Ravishankara, Chem. Phys. Lett. **242**(4-5), 427–434 (1995).
[63]D. Hölscher, C. Fockenberg, and R. Zellner, Phys. Chem. **102**(5), 716–722 (1998).
[64]W. J. Bloss, T. J. Gravestock, D. E. Heard, T. Ingham, G. P. Johnson, and J. D. Lee, J. Environ. Monit. **5**(1), 21–28 (2003).
[65]T. J. Gravestock, M. A. Blitz, and D. E. Heard, Phys. Chem. Chem. Phys. **7**(10), 2173–2181 (2005).
[66]S. M. Newman, W. H. Howie, I. C. Lane, M. R. Upson, and A. J. Orr-Ewing, J. Chem. Soc., Faraday Trans. **94**(18), 2681–2688 (1998).
[67]T. J. Gravestock, M. A. Blitz, and D. E. Heard, Phys. Chem. Chem. Phys. **12**(4), 823–834 (2010).
[68]M. L. P. Rao, D. V. K. Rao, and P. T. Rao, Phys. Lett. A **50**(5), 341–342 (1974).
[69]See supplementary material at http://dx.doi.org/10.1063/1.4869857 for brief description of the relevant details.
[70]R. M. Stimpfle, D. M. Wilmouth, R. J. Salawitch, and J. G. Anderson, J. Geophys. Res., [Atmos.] **109**(D3), D03301, doi:10.1029/2003JD003811 (2004).
[71]W. H. Brune, J. G. Anderson, and K. R. Chan, J. Geophys. Res., [Atmos.] **94**(D14), 16639–16647 (1989).
[72]T. M. Hard, R. J. Obrien, C. Y. Chan, and A. A. Mehrabzadeh, Environ. Sci. Technol. **18**(10), 768–777 (1984).
[73]M. K. Gilles, A. A. Turnipseed, R. K. Talukdar, Y. Rudich, P. W. Villalta, L. G. Huey, J. B. Burkholder, and A. R. Ravishankara, J. Phys. Chem. **100**(33), 14005–14015 (1996).
[74]S. P. Sander, J. Abbatt, J. R. Barker, J. B. Burkholder, R. R. Friedl, D. M. Golden, R. E. Huie, C. E. Kolb, M. J. Kurylo, G. K. Moortgat, V. L. Orkin, and P. H. Wine, in *JPL Publication 10-6*, edited by J. P. Laboratory (Pasadena, CA, 2011).
[75]M. A. A. Clyne and L. G. Piper, J. Chem. Soc., Faraday Trans. 2 **72**, 2178–2190 (1976).
[76]R. E. Stickel, A. J. Hynes, J. D. Bradshaw, W. L. Chameides, and D. D. Davis, J. Phys. Chem. **92**(7), 1862–1864 (1988).
[77]M. Eastwood and R. Zechman, private communication (2011).
[78]S. La Barre, P. Potin, C. Leblanc, and L. Delage, Mar. Drugs **8**(4), 988–1010 (2010).
[79]R. M. Chambers, A. C. Heard, and R. P. Wayne, J. Phys. Chem. **96**(8), 3321–3331 (1992).
[80]N. Kaltsoyannis and J. M. C. Plane, Phys. Chem. Chem. Phys. **10**(48), 1723–1733 (2008).
[81]S. Madronich and S. J. Flocke, in *Handbook of Environmental Chemistry*, edited by P. Boule (Springer, Heidelberg, 1999), pp. 1–26.
[82]L. G. Harris and M. C. Tyrrell, Biol. Invasions **3**, 9–21 (2001).
[83]R. J. Huang, U. R. Thorenz, M. Kundel, D. S. Venables, D. Ceburnis, K. F. Ho, J. Chen, A. L. Vogel, F. C. Kupper, P. P. A. Smyth, U. Nitschke, D. B. Stengel, H. Berresheim, C. D. O'Dowd, and T. Hoffmann, Atmos. Chem. Phys. **13**(10), 5255–5264 (2013).
[84]Y. Kanaya, Y. Yokouchi, J. Matsumoto, K. Nakamura, S. Kato, H. Tanimoto, K. Toyota, and H. Akimoto, Geophys. Res. Lett. **29**(8), 45, doi:10.1029/2001GL014061 (2002).